

# Experiments on passive hypersonic boundary layer control using ultrasonically absorptive carbon–carbon material with random microstructure

Alexander Wagner · Markus Kuhn ·  
Jan Martinez Schramm · Klaus Hannemann

Received: 5 March 2013/Revised: 1 August 2013/Accepted: 23 September 2013/Published online: 10 October 2013  
© Springer-Verlag Berlin Heidelberg 2013

**Abstract** For the first time, the influence of ultrasonically absorptive carbon–carbon material on hypersonic laminar to turbulent boundary layer transition was investigated experimentally. A  $7^\circ$  half-angle blunted cone with a nose radius of 2.5 mm and a total length of 1,077 mm was tested at zero angle of attack in the High Enthalpy Shock Tunnel Göttingen of the German Aerospace Center (DLR) at Mach 7.5. One-third of the metallic model surface in circumferential direction was replaced by DLR in-house manufactured ultrasonically absorptive carbon–carbon material with random microstructure for passive transition control. The remaining model surface consisted of polished steel and served as reference surface. The model was equipped with coaxial thermocouples to determine the transition location by means of surface heat flux distribution. Flush-mounted piezoelectric fast-response pressure transducers were used to measure the pressure fluctuations in the boundary layer associated with second-mode instabilities. The free-stream unit Reynolds number was varied over a range of  $Re_m = 1.5 \times 10^6 \text{ m}^{-1}$  to  $Re_m = 6.4 \times 10^6 \text{ m}^{-1}$  at a stagnation enthalpy of  $h_0 \approx 3.2 \text{ MJ/kg}$  and a wall temperature ratio of  $T_w/T_0 \approx 0.1$ . The present study

revealed a clear damping of the second-mode instabilities and a delay of boundary layer transition along the ultrasonically absorptive carbon–carbon insert.

## 1 Introduction

Laminar to turbulent transition in high-speed boundary layers leads to a significant increase in wall shear stress and wall heat flux. Thus, the performance and the thermal protection system of hypersonic vehicles are strongly affected. The increase in the laminar portion of the boundary layer is of critical importance to the design and optimization of these vehicles (Force 1992). This motivates the development of hypersonic laminar flow control concepts.

For small free-stream disturbances and negligible surface roughness, the second-mode instability is the dominant instability in predominantly two-dimensional boundary layers at hypersonic speeds (Malik 1989). Wall temperatures below the recovery temperature as present e.g., on hypersonic vehicles are known to stabilize the first-mode and to destabilize the second-mode instability. Both facts serve as basis for the concept developed by Fedorov et al. (2001) and Malmuth et al. (1998) to passively control transition on hypersonic vehicles using ultrasonically absorptive surfaces. The hypothesis that such materials can massively reduce the amplification rate of the second-mode by absorbing the disturbance energy and thus to delay the transition onset was shown theoretically by Fedorov et al. (2001) using linear stability theory. Rasheed et al. (2002) experimentally confirmed the stabilizing effect by showing a delay of the transition onset using a porous surface with regularly spaced cylindrical blind holes on a sharp  $5^\circ$  half-angle cone at Mach 5 in the T-5 High Enthalpy Shock

---

A. Wagner (✉) · J. Martinez Schramm · K. Hannemann  
German Aerospace Center (DLR), Institute of Aerodynamics and  
Flow Technology, Göttingen, Germany  
e-mail: alexander.wagner@dlr.de

J. Martinez Schramm  
e-mail: Jan.Martinez@dlr.de

K. Hannemann  
e-mail: Klaus.Hannemann@dlr.de

M. Kuhn · J. Martinez Schramm · K. Hannemann  
German Aerospace Center (DLR), Institute of Structures and  
Design, Stuttgart, Germany  
e-mail: Markus.Kuhn@dlr.de

Tunnel of the California Institute of Technology. It was demonstrated that if the pore size is significantly smaller than the viscous length scale, a porous surface is highly effective in delaying second-mode dominated boundary layer transition. Further studies on ultrasonically absorptive surfaces with regular microstructure were conducted by Fedorov et al. (2006) in the ITAM T-326 Mach 6 hypersonic wind tunnel on a  $7^\circ$  half-angle sharp cone. Hot-wire measurements conducted in the scope of these studies revealed that the porous surface weakly amplifies the first-mode, due to the surface roughness, but stabilizes the second-mode which was identified to be the dominant instability.

Analogous measurements using a thin coating of fibrous absorbent material (felt metal) with random microstructure were carried out by Fedorov et al. (2003). The material is of particular interest since its random microstructure is typical for practical TPS (thermal protection system) materials. Hot-wire measurements in the laminar boundary layer revealed a reduction in the second-mode instability and thus the potential to delay transition onset. Maslov et al. (2006, 2008) confirmed the assumption by showing a significant increase in laminar run on a sharp  $7^\circ$  half-angle cone which was equipped with felt metal and tested in the AT-303 ITAM wind tunnel at Mach 12 and in the ITAM impulse hypersonic wind tunnel Transit-M at Mach 6.

The cavity depth and the surface porosity were numerically identified as the parameters dominating the effectiveness of the porous surface (Brès et al. 2010; Wartemann et al. 2012a). In particular, the impact of the pore depth was investigated experimentally by Lukashovich et al. (2012). A pore depth about 50 % higher compared to the effective pore diameter was found as an optimum. The optimal porous layer thickness leads to a phase cancelation and thus to maximum stabilization of the second-mode waves. A further increase in the pore depth leads to a decrease in the stabilization and finally tends toward the deep pore limit (Wartemann et al. 2012b).

Based on the promising results obtained on porous surfaces with regular and random microstructures and based on the fact that the majority of the TPS materials have random microstructures, a material with practical TPS potential was used for the first time for passive transition control. Hence, carbon fiber reinforced carbon (C/C) was chosen as model material to assess the potential of ceramic matrix composites. It represents an intermediate state of C/C-SiC which has been successfully used as TPS on hypersonic vehicles (Turner et al. 2006; Weihs et al. 2008). C/C material is lightweight and offers high-temperature stability in absence of oxygen, but might need to be adapted for real TPS applications to improve its oxidation resistance. Previous experimental studies on  $7^\circ$  half-angle blunted cones in the DLR High Enthalpy Shock

Tunnel Göttingen (HEG) at Mach 7.4 confirmed that the transition process is dominated by the second-mode instability (Wagner et al. 2011; Laurence et al. 2012; Wagner et al. 2012). The HEG conditions used in these studies served as baseline test environment for the present investigations.

The present article focuses on the design and the manufacturing of the wind tunnel model and in particular on the manufacturing and characterization of the carbon-carbon material. Boundary layer disturbances on the model were measured by means of surface pressure fluctuations for a range of unit Reynolds numbers. A stabilization of the second-mode instability and an increase in the laminar portion of the boundary layer on the porous surface was observed.

## 2 High Enthalpy Shock Tunnel Göttingen (HEG)

The HEG was commissioned for use in 1991. Since then it has been used extensively in a large number of national and international space and hypersonic flight projects. Originally, the facility was designed for the investigation of the influence of high-temperature effects such as chemical and thermal relaxation on the aerothermodynamics of entry or reentry space vehicles. In this operating range, total specific enthalpies of up to 23 MJ/kg and nozzle stagnation pressures of up to 150 MPa can be reached. In recent years, its range of operating conditions has been subsequently extended, the main emphasis being to generate new test conditions which allow investigating the flow past hypersonic flight configurations from low altitude Mach 6 up to Mach 10 at approximately 33 km altitude (Hannemann and Martinez Schramm 2007; Hannemann et al. 2008).

An overview of the HEG shock tunnel is provided by the schematic in Fig. 1. The overall length and mass of the facility are 60 m and 280 t, respectively. The shock tunnel

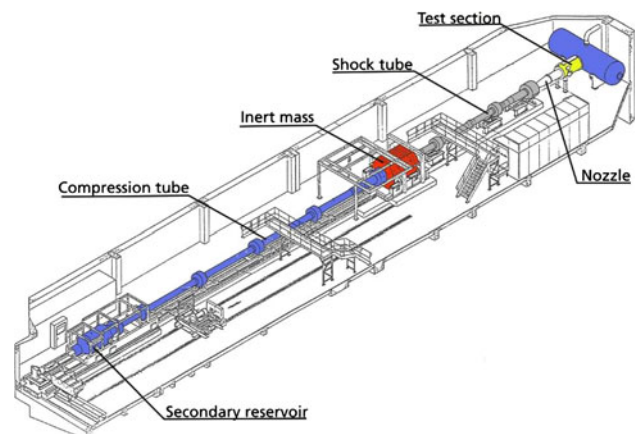


**Fig. 1** Schematic (left) and photographic views (right) of HEG

consists of a secondary reservoir, a compression tube, separated from an adjoining shock tube by the primary diaphragm, and a subsequent nozzle and test section. For a test in HEG pressurized air in the secondary reservoir is used to accelerate the piston down the compression tube. The driver gas in the compression tube is compressed quasi-adiabatically. When the burst pressure is reached, the main diaphragm ruptures and hot high-pressure gas expands into the shock tube. The shock wave produced is reflected at the end wall and provides the high-pressure, high-temperature gas which is expanded through a contoured convergent–divergent hypersonic nozzle after secondary diaphragm rupture.

In the scope of the present article, HEG has been operated at the conditions listed in Table 1, i.e., in a free-stream unit Reynolds number range between  $1.4 \times 10^6$  and  $6.4 \times 10^6 \text{ m}^{-1}$  and low total enthalpies around 3 MJ/kg. Typical test times for these conditions range between 2.5 and 3 ms.

### 3 Experimental setup

#### 3.1 Model and instrumentation

The model is a  $7^\circ$  half-angle blunted cone with an overall length of 1,077 mm and an exchangeable nose tip. For the present experiments, a nose radius of 2.5 mm radius was used. The model is equipped with a 835-mm-long insert for the integration of an ultrasonically absorptive carbon–carbon (C/C) material. The insert starts at 182 mm from the model tip and covers  $122^\circ$  of the model surface in circumferential direction. Figure 2 shows the basic dimensions of the model. Special attention was paid to the model surface quality. To minimize potential discontinuities at junctions, the model was machined with the C/C insert installed. The nose tip has been pre-machined separately and fitted to the main model by hand. The main model and the model tip were manufactured from stainless steel (RAMAX2<sup>®</sup>). The smooth surface of the model was finished using ISO P1500 sandpaper, corresponding to an average particle diameter of 12.6  $\mu\text{m}$ .

**Table 1** Operating conditions of the presented study in HEG

$Re_m \text{ (m}^{-1}\text{)}$	$1.5 \times 10^6$	$4.0 \times 10^6$	$6.4 \times 10^6$
$p_0 \text{ (MPa)}$	6.7	19	28
$T_0 \text{ (K)}$	2,690	2,720	2,550
$H_0 \text{ (MJ/kg)}$	3.2	3.2	3.0
$T_\infty \text{ (K)}$	260	270	245
$\rho_\infty \text{ (g/m}^3\text{)}$	10	28	42
$u_\infty \text{ (m/s)}$	2,400	2,410	2,340

The tested model was equipped with 49 flush-mounted coaxial thermocouples of type E<sup>1</sup> with a spacing of 33.3 mm to measure the transition location by means of surface heat flux evaluation. Thereof, 24 transducers were installed along the center ray on the porous model surface, i.e., the upper model boundary shown in Fig. 2 on the right, and 25 along a ray directly opposite on the smooth surface with the identical  $x$ -coordinates starting at 190 mm downstream the model tip. Furthermore, 12 piezoelectric PCB132A32 fast-response pressure transducers were flush mounted along the model on the smooth surface at  $x = 632 \text{ mm}$ ,  $x = 767 \text{ mm}$ ,  $x = 947 \text{ mm}$  and on the porous surface at  $x = 632 \text{ mm}$ ,  $x = 767 \text{ mm}$ ,  $x = 932 \text{ mm}$  from the nose tip at  $48^\circ$ ,  $-20^\circ$  and  $15^\circ$  from the center ray, see Fig. 2 right. These pressure transducers have a sensitive surface diameter of 3.18 mm and cover a frequency range of 11 kHz to 1 MHz. A sampling rate of 10 MHz resulted in a frequency resolution of around 0.2 kHz for the HEG test conditions provided in Table 1. The transducers were used to measure pressure fluctuations in the boundary layer associated with second-mode instabilities. Piezoelectric type pressure transducers are sensitive to accelerations. For this reason, the pressure transducers were installed using a silicone shroud to mechanically decouple the transducers from the model and thus to reduce the transfer of high frequency vibrations from the model to the transducer. Reference pressure transducers of the same type mounted inside the model, and therefore not exposed to the flow, were used at each PCB transducer location. The reference transducers were used to eliminate from the measured signals the contribution caused by mechanical vibrations not associated with pressure fluctuations in the boundary layer if necessary. The maximum misalignment of the PCB pressure transducers was estimated to be below 0.3 mm. Additionally, 8 pressure transducers of type KULITE XCL-100-100A were installed adjacent to the PCB transducer location and at 182 and 402 mm from the tip on the smooth surface to measure the surface pressure distribution along the model. The transducer positions on the model were chosen based on the experience gathered in previous transition studies on cone models in HEG (Wagner et al. 2011).

The model was supported by a sting system at its base at nominal zero angle of attack.

#### 3.2 Ultrasonically absorptive material

About one-third of the stainless steel surface was replaced by a carbon fiber reinforced carbon ceramic (C/C). This

<sup>1</sup> ASTM Standard E 230-96, Standard Specification and Temperature-Electromotive Force (EMF) Tables for Standardized Thermocouples, Annual Book of ASTM Standards 14.03, 106, Amer. Soc. for Test. And Matls., Philadelphia, PA (1997).

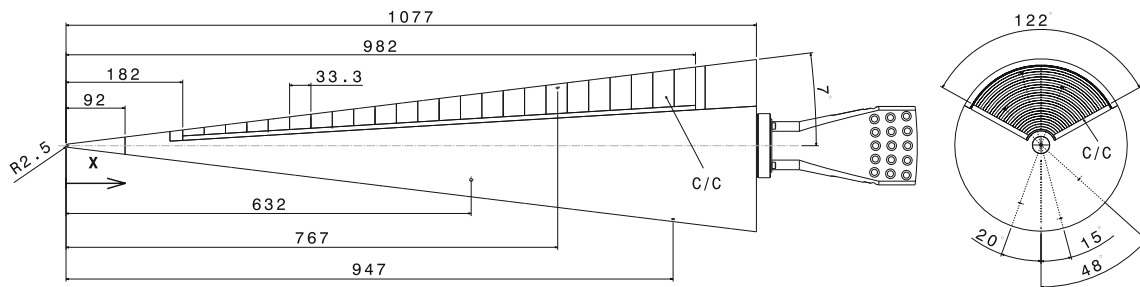


**Fig. 2** HEG wind tunnel model; dimensions in mm

material represents an intermediate state obtained during the C/C-SiC manufacturing process (Krenkel 2003). In order to reach this state, the following steps are conducted: By means of an autoclave technique, a green body of carbon fiber reinforced plastic (CFRP) is formed using commercially available 0°/90° carbon fiber fabrics impregnated with a phenolic resin. After curing, the green body is pyrolyzed at temperatures of up to 1,650 °C, which converts the phenolic matrix to amorphous carbon. This results in a C/C body containing random patterns of micro-cracks. Carbon fiber reinforced carbon offers low thermal expansion and specific weight as well as high-temperature stability in absence of oxygen. Its structure can be very well reproduced during the manufacturing process and has already been applied widely for, e.g., coated leading edges of hypersonic vehicles (Glass et al. 2006; Glass 2008) and transpiration cooled combustion chamber applications (Hald et al. 2009; Ortel et al. 2010).

The manufacturing of the type of C/C material applied here is based on stacking 0°/90° carbon fiber fabrics. Hence, the material exhibits an orthotropic layout, as depicted in Fig. 3. This is associated with a different thermo-mechanical behavior in longitudinal (1, 2) and transverse (3) direction with respect to the carbon fiber fabrics. The computer tomography picture shows the resulting micro-crack system with a random distribution. The symbol ∞ indicates the free-stream direction during the wind tunnel tests relative to the C/C material. In total, seven plates of C/C material were manufactured and used for the ceramic insert. For each plate, open porosities and raw densities have been determined by a gravimetric analysis according to DIN EN 993-1. Thereby, the open porosity is defined by the ratio of open pore volume to total volume. This results in an averaged open porosity of  $14.98 \pm 0.24 \%$  and density of  $1.3304 \pm 0.0031 \text{ g/cm}^3$ , as shown in Fig. 4.

In order to get a better understanding of the occurring pore geometries, the pore size distribution of the applied C/C material was determined by means of mercury intrusion porosimetry. Therefore, a sample was placed into a sample cell, which was evacuated. Non-wetting mercury was inserted, and pressure was applied to force the mercury penetrating the sample. At lower pressures, only bigger

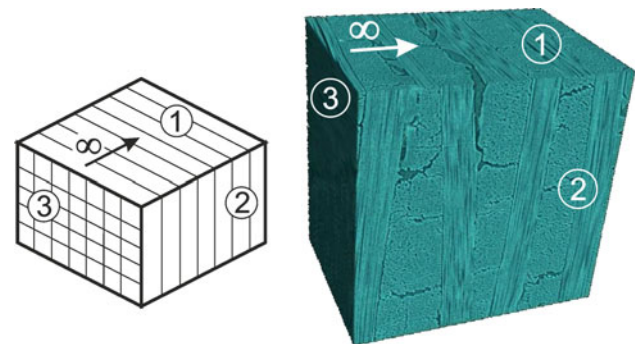


**Fig. 3** Schematic (left) and computer tomography (right) picture of the applied C/C material

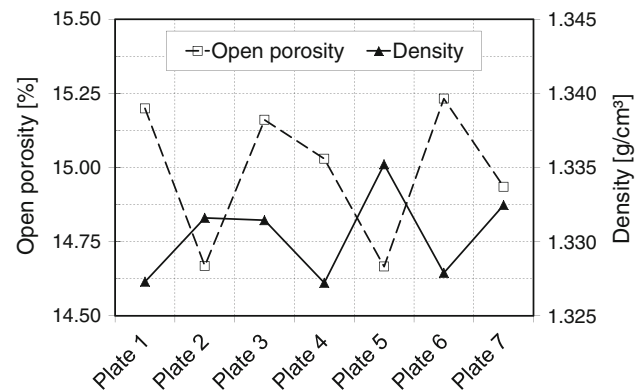


**Fig. 4** Measured density and porosity of manufactured C/C plates used for model insert

pores of the material were filled, whereas at higher pressures, smaller pores were intruded. A maximum pressure of up to 200 MPa was applied leading to a fully mercury intruded material. The relation between the applied pressure  $p$  and the volume of mercury intruded into the sample is recorded. By means of the Washburn equation, the applied pressure can be correlated with cylindrically shaped pores with diameter  $D$  (Washburn 1921):

$$D = - \frac{4\gamma \cos \theta}{p} \quad (1)$$

with  $\gamma$  and  $\theta$  being the mercury surface tension and contact angle, respectively. In general, this equation is also used to



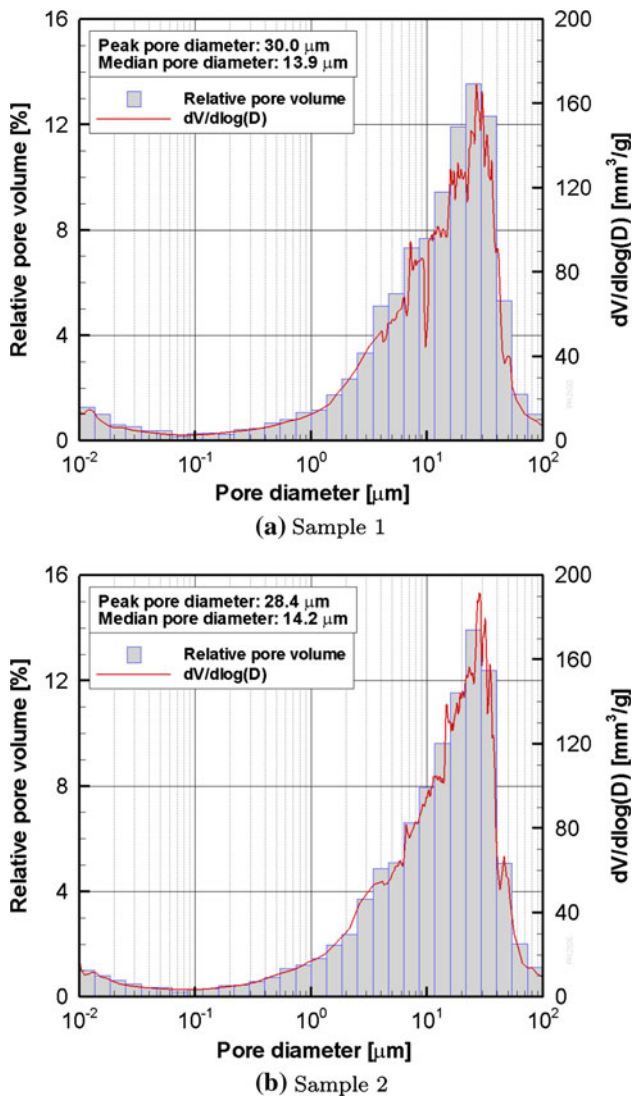


**Fig. 5** C/C pore size distributions

describe materials having non-cylindrical pores, such as the present C/C material consisting of micro-cracks and slitlike pore shapes.

Hence, the pore size distribution as a function of pore volumes and pore diameters can be detected. The pore size distribution has been determined in the pore diameter range 0.01–100  $\mu\text{m}$ , pore sizes beyond that range cannot be detected with the facility used. Figure 5 shows histograms of the material's pore size distributions. The relative pore volume characterizes the volume of defined pore diameter ranges with respect to the total volume of mercury intruded into the C/C sample. Furthermore, the corresponding derivative  $dV/d\log(D)$  of intruded pore volume with respect to the logarithm of the pore diameter is shown. The plots show the measured pore size distribution for two out of four samples, taken from four different C/C plates. This allows to determine peak and median pore (calculated at 50 % of total pore volume) diameters, ranging between 28–30

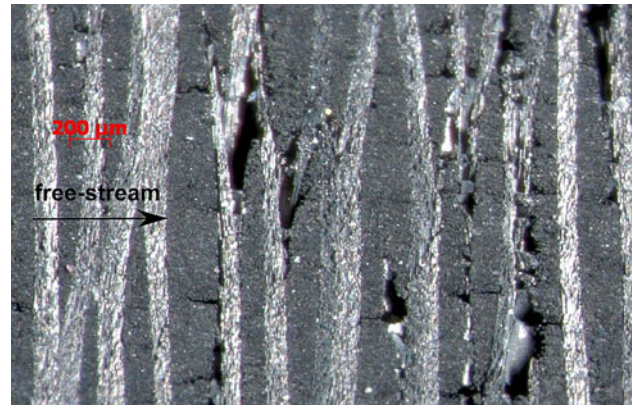


**Fig. 6** Optical microscopy image of C/C surface showing intact structure after completion of the test campaign in HEG, 60 $\times$  magn

and 11–14  $\mu\text{m}$ , respectively. All samples show a similar and comparable distribution. It can be stated that there is no single dominant pore diameter, but rather a distinctive pore system for pore diameters between approximately 1 and 100  $\mu\text{m}$ . Pores mainly occur in the matrix, whereas bigger pore diameters are connected to micro-cracks which result from the shrinking of the matrix during the manufacturing process.

### 3.3 Model insert design, manufacturing and integration

Taking the orthotropic properties of the C/C material into account, the porous material was aligned such that the layers were oriented perpendicular [planes (1, 2) in Fig. 3]) to the free-stream direction. As the crack propagation along the layers is dominant, this results in infinite micro-crack systems deeply penetrating the ceramic material. Figure 6 shows an optical microscopy image of the C/C surface after test campaign completion. Two design requirements of the model were to provide sufficient internal space for transducer integration and the replaceability of the insert. Hence, a combined setup of ceramic insert parts and a supporting aluminum (EN AW7075) subframe structure, as shown in Fig. 7, was used. The substructure consists of two side brackets, a back bracket and a support with eight cylindrical segments with increasing diameter in stream-wise direction.

On each cylindrical section of the support, three ceramic parts were placed which resulted in a total of 24 C/C parts. Consequently, the C/C thickness varies between 5 and 17 mm which corresponds to the maximum penetrating pore depth. The design enables to integrate right-angled parts and to avoid an inner tapered surface. Furthermore, the ceramic parts' inner contour on each cylindrical section of the support remains constant which simplifies the manufacturing process. The manufacturing of the porous model insert involved the production of seven C/C plates

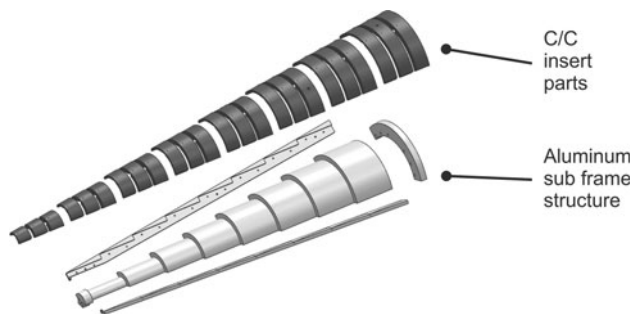


**Fig. 7** Ceramic model insert setup



**Fig. 8** Single CNC milled C/C parts (*top*) and model insert with bonded ceramic parts (*bottom*)

with a dimension of 250 mm × 200 mm × 40 mm. Those plates were ground to a thickness of  $33.44 \pm 0.01$  mm. Subsequently, the coarse contours of 24 single C/C parts and additional spares were prepared by means of water jet cutting. In the next step, the inner contour of each part was milled using a CNC machine (see Fig. 8) to fit onto the subframe structure. Three identical parts were manufactured for each cylindrical section of the support. All ceramic segments were clamped onto the insert using the two side brackets. Additionally, each segment was bonded onto the aluminum substructure by means of a fast-curing adhesive resin to take possible shock loads during the tests into account and to provide a rigid structure for the final surface manufacturing. Tests were performed to check whether the adhesive resin penetrates the C/C microstructure due to capillary forces and thus reduces the effective material thickness. Therefore, a C/C sample with a

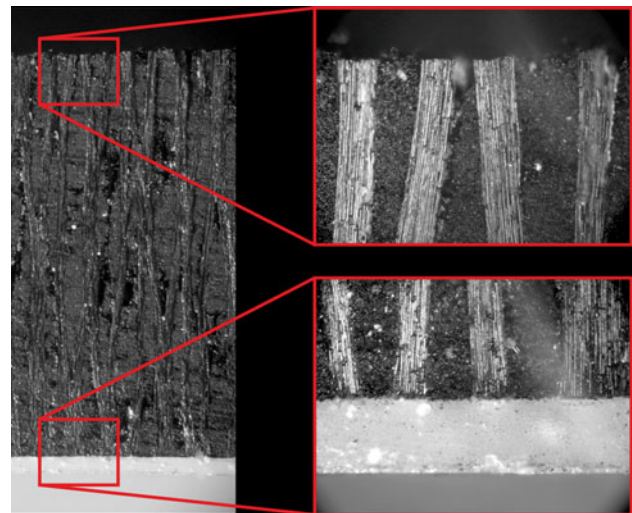


**Fig. 9** Bonding tests: optical microscopy images showing marginal penetration of the adhesive resin (*white layer*) into the micro-pore structure: Free-stream (*top*) and bonded side (*bottom*), ×200 magn

thickness of 5 mm, which corresponds to the minimum insert thickness, was bonded onto a metallic sheet. After curing, the sample was cut and analyzed via optical microscopy. As depicted in Fig. 9, no significant penetration of the adhesive into the porous C/C material could be observed.

All C/C parts were bonded onto the metallic support and fixed to the subframe structure as shown in Fig. 8. To ensure a tight fit, the ceramic parts were compressed via the metallic back bracket by approximately 2.5 mm over the entire ceramic parts' length of 800 mm. Afterward, this assembly was cured at elevated temperatures according to the adhesive resin specifications.

In the next step, the ceramic insert was integrated into the cone model and the whole setup was finished by means of ultrasonic milling to account for a high surface quality of both the ceramic and the metallic model surfaces. Afterward, the insert was removed and cleaned in an ultrasonic bath to remove milling debris from the surface and the pores. Finally, all sensors of the porous insert were installed, and the ceramic insert was integrated into the cone model, as depicted in Fig. 10.

Since the test section of HEG is evacuated before each run, a characteristic time is required until the pressure in the C/C pores equals the static pressure on the model surface. To ensure the porous surface to be effective in a short-duration test facility such as HEG, the characteristic pore filling time has to be small compared to the test time. The flow in the HEG test section is initiated by the incident shock followed by the nozzle starting process. At the time the shock passes over the model surface, the pressure in the pores is much smaller compared to the post-shock pressure. Therefore, the flow into the pore volume is assumed to be

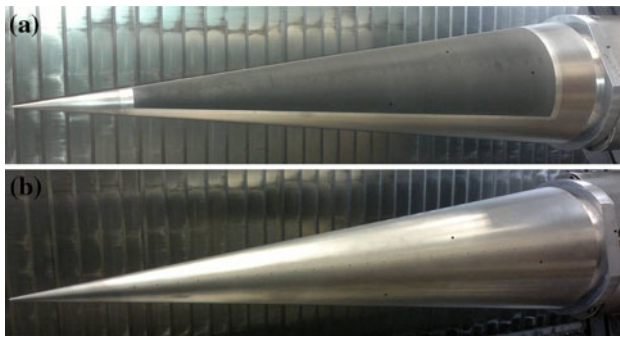


**Fig. 10** Fully integrated cone model. **a** Porous insert. **b** Stainless steel reference surface

initially choked. Based on this assumption, the rate of pressure rise can be estimated up to the point in time when the pressure ratio is not sufficient anymore to choke the flow. In the subsequent time period, neglecting compressibility effects, the rate of pressure rise was assumed to be proportional to the pressure difference. Furthermore, assuming a homogeneous porosity, a maximum pore depth of 17 mm was assumed corresponding to the maximum C/C thickness. The time required to reach a pressure inside the pores equal to 99 % of the ambient pressure was estimated to be 0.37 ms. Viscous effects which lead to an effectively smaller pore diameter and thus to a higher pore filling time were not considered. The estimated pore filling time is about a factor of 5 lower than the nozzle start up time corresponding to the HEG test conditions presented in Table 1. Based on these results, it was concluded that an equilibrium situation between the static pressure in the free-stream and inside the pores was established before the test time period starts.

#### 4 Results

A series of tests at unit Reynolds numbers between  $Re_m = 1.5 \times 10^6 \text{ m}^{-1}$  and  $Re_m = 6.4 \times 10^6 \text{ m}^{-1}$  were conducted. Figure 11 shows the Stanton number distribution versus the free-stream Reynolds number based on the model  $x$ -coordinate, originating at the model tip and pointing downstream along the center line. The Stanton number is defined as follows:

$$St = \frac{\dot{q}_w}{\rho_e U_e (h_0 - h_w)} \quad (2)$$

with  $\dot{q}_w$  being the measured specific wall heat flux,  $\rho_e$  and  $U_e$  the density and velocity at the boundary layer edge and  $h_0$  the total specific enthalpy. The specific enthalpy at the wall  $h_w$  is small compared to  $h_0$  and thus is neglected.

A clear shift of the transition onset toward higher Reynolds numbers is observed on the porous surface for

$Re_m = 4.0 \times 10^6 \text{ m}^{-1}$  and  $Re_m = 6.4 \times 10^6 \text{ m}^{-1}$ . At a unit Reynolds number of  $Re_m = 4.0 \times 10^6 \text{ m}^{-1}$ , the transition Reynolds number increases from  $Re_t = 2.7 \times 10^6$  to about  $Re_t = 3.0 \times 10^6$ . The relative transition delay appears to be higher at a unit Reynolds number of  $Re_m = 6.4 \times 10^6 \text{ m}^{-1}$  with a transition Reynolds number of  $Re_t = 3.0 \times 10^6$  on the smooth surface and  $Re_t = 3.9 \times 10^6$  on the porous surface. The transition onset location was defined at the first transducer showing a significant heat flux increase above the predicted laminar level followed by transducers showing a clear heat flux increase toward a turbulent boundary layer.

On the porous surface, the heat flux scatter around the predicted laminar and turbulent heat flux levels is higher compared to the smooth surface as shown in 11 and 13. It is assumed that the scattering is caused by small transducer misalignments on the model surface. In contrast to the smooth steel surface, the thermocouples cannot be integrated into the C/C material by grinding the transducer head. Therefore, the transducers are aligned by hand and thus subject to small misalignment which possibly leads to the observed scatter.

Figure 12 shows the power spectral density (PSD) of the flush-mounted PCB132A32 pressure transducers at a unit Reynolds number of  $Re_m = 1.5 \times 10^6 \text{ m}^{-1}$ . This is the only test condition for which second-mode waves could be detected at all three transducer locations. The signals were smoothed in the frequency domain using a Savitzky-Golay filter of sixth-order and a length of 251 samples. On the smooth surface, a second-mode peak forms at 260 kHz at the most upstream position. The peak increases in downstream direction, whereas its maximum is shifted to lower frequencies, i.e., 220 kHz at  $x/L = 0.71$ . At the most downstream transducer location, the peak broadened without further increase in amplitude which indicates second-mode breakdown and thus the forming of turbulent spots. This results in a heat flux increase further downstream the transducer position which can be observed in Fig. 11 (the PCB transducer position corresponds to  $Re_x = 1.3 \times 10^6$ ). In contrast, on the porous surface, second-mode peak frequencies of 247 and 227 kHz are measured at the first two transducer locations. Both peaks are significantly lower in amplitude compared to the smooth surface measurements. Furthermore, the increase in the second-mode peak between the two transducer locations amounts to only 32 % compared to 116 % on the smooth surface, based on the amplitude at the first transducer location. Thus, the second-mode instability appears to be significantly damped on the porous surface. However, at the most downstream transducer location, a second-mode peak at 200 kHz forms with an amplitude indicating a very high instability growth rate between  $x/L = 0.71$  and  $x/L = 0.86$ .



**Fig. 11** Normalized heat flux distribution on porous and smooth surface for different unit Reynolds numbers (transition Reynolds numbers marked by circles)

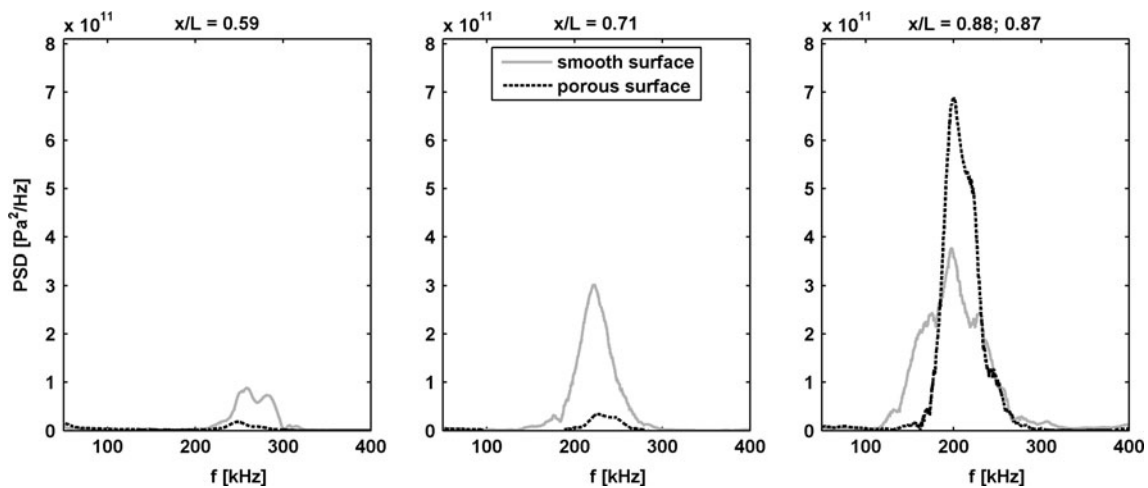
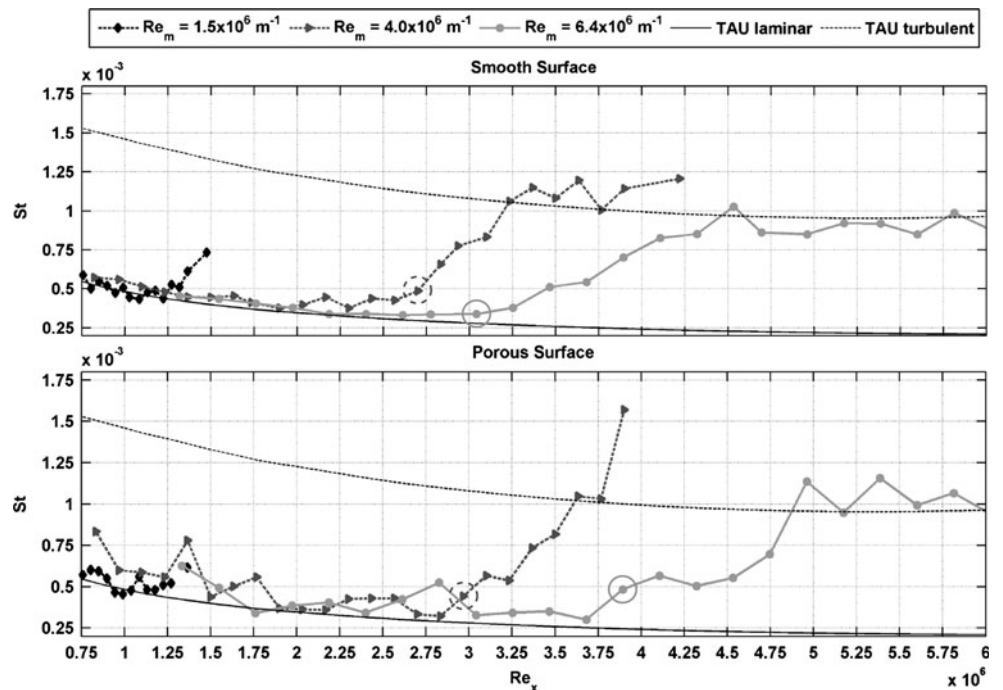


**Fig. 12** PSD of the pressure fluctuations on the smooth and the porous surface,  $Re_m = 1.5 \times 10^6 \text{ m}^{-1}$

The transition location on cone models might be affected by angle of attack variations, e.g., reported by Willems and Gülhan (2012). Therefore, additional tests were conducted to study the effect of small deviations from the nominal AOA = 0° which might be caused by model misalignment. The angle of attack of the model in HEG was adjusted using an inclinometer with a measuring error below 0.027°. In two subsequent tests, the angle of attack was varied in a range of ±0.2° which is above the uncertainty of the inclinometer used. Figure 13 shows the normalized heat flux distributions on the porous and the smooth surface for these two runs. No significant changes of the transition location on both surfaces is visible.

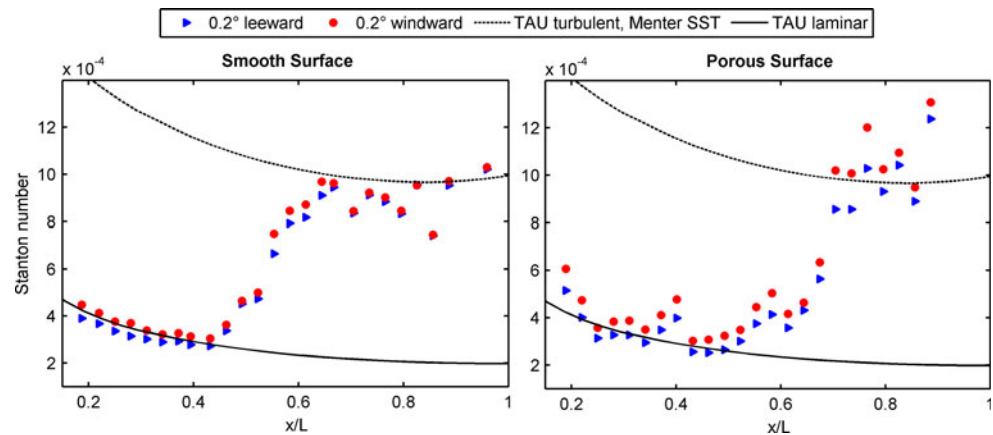
Therefore, it can be concluded that angles of attack in the order of ±0.2° do not influence the above discussed results.

### 5 Summary

For the first time, hypersonic boundary layer transition was investigated on a 7° half-angle cone with ultrasonically absorptive C/C material representing a potential TPS material. The material properties and the model manufacturing are described in detail in the present article. The porous surface has a random microstructure with a peak pore diameter of 28–30 μm and a porosity of 15 %. By



**Fig. 13** Normalized heat flux distribution for a AOA variation of  $\pm 0.2^\circ$  at  $Re_m = 6.4 \times 10^6 \text{ m}^{-1}$



means of surface pressure fluctuation measurements, the damping of the second-mode instability above the porous surface was shown. Furthermore, a clear delay of the transition onset was observed by means of surface heat flux measurements. A study of the impact of small angle of attack variations revealed that deviations in the range of  $\pm 0.2^\circ$  do not have an impact on the transition location in the present experiments.

The present study confirmed the potential of ultrasonically absorptive carbon-carbon material to be applicable to passively control hypersonic boundary layer transition. The obtained results are in line with the transition delay observed in previous studies on randomly structured felt metal at ITAM. The presented results show a dependency of the C/C efficiency on the Reynolds number. The transition delay increases with increasing unit Reynolds number. This indicates that the C/C properties are not optimal for the test conditions applied, i.e., the surface porosity and the average pore size are too small. A further development of the material to improve the ultrasonically absorptive properties is conceivable by adapting the phenolic resin composition to optimize the pore size distribution. Fedorov et al. (2008) proposed a procedure to experimentally determine the acoustic properties of porous coatings, in terms of the reflection coefficient, which could be used to evaluate such porous materials to support the optimization process.

**Acknowledgments** The presented work was conducted in the framework of the DLR project *IMENS-3C*. The authors wish to thank Frank Entenmann of the Institute of Structures and Design (DLR) for the manufacturing of the C/C insert. The support provided by Stuart Laurence and the HEG team during the test campaign is highly appreciated.

## References

- Brès GA, Colonius T, Fedorov AV (2010) Acoustic properties of porous coatings for hypersonic boundary-layer control. *AIAA J* 48(2):267–274. doi:10.2514/1.40811
- Fedorov A, Shipliyuk A, Maslov A, Burov E, Malmuth N (2003) Stabilization of a hypersonic boundary layer using an ultrasonically absorptive coating. *J Fluid Mech* 479:99–124. doi:10.1017/S0022112002003440
- Fedorov A, Kozlov V, Shipliyuk A, Maslov A, Malmuth N (2006) Stability of hypersonic boundary layer on porous wall with regular microstructure. *AIAA J* 44(8):1866–1871
- Fedorov AV, Malmuth ND, Rasheed A, Hornung HG (2001) Stabilization of hypersonic boundary layers by porous coatings. *AIAA* 39(4):605–610
- Fedorov AV, Kozlov VF, Addison RC (2008) Reflection of acoustic disturbances from a porous coating of regular microstructure. In: 5th AIAA theoretical fluid mechanics conference, AIAA 2008-3902
- Force NT (1992) Report of the defense science board task force on the national aerospace plane (NASP). Tech. rep., Defense Science Board, Office of the Secretary of Defense, Washington, D.C. 20301-3140
- Glass D, Dirling R, Croop H, Fry TJ, Frank GJ (2006) Materials development for hypersonic flight vehicles. In: 14th AIAA/AHI space planes and hypersonic systems and technologies conference, Canberra, AIAA 2006-8122
- Glass DE (2008) Ceramic matrix composite (CMC) thermal protection systems (TPS) and hot structures for hypersonic vehicles. In: 15th AIAA space planes and hypersonic systems and technologies conference, Dayton, OH, AIAA 2008-2682
- Hald H, Herbertz A, Kuhn M, Ortelt M (2009) Technological aspects of transpiration cooled composite structures for thrust chamber applications. In: 16th AIAA/DLR/DGLR international space planes and hypersonic systems and technologies conference, Bremen, AIAA 2009-7222
- Hannemann K, Martinez Schramm J (2007) High enthalpy, high pressure short duration testing of hypersonic flows. In: Springer handbook of experimental fluid mechanics. Springer, Berlin
- Hannemann K, Martinez Schramm J, Karl S (2008) Recent extensions to the High Enthalpy Shock Tunnel Göttingen (HEG). In: Proceedings of the 2nd international ARA days 'ten years after ARD', Arcachon, France
- Krenkel W (2003) Applications of fibre reinforced C/C-SiC ceramics. *Ceram Forum Int* 80(8):31–38
- Laurence S, Wagner A, Hannemann K, Wartemann V, Lüdeke H, Tanno H, Ito K (2012) Time-resolved visualization of instability waves in a hypersonic boundary layer. *AIAA J* 50(1):243–246. doi:10.2514/1.J051112
- Lukashevich SV, Maslov AA, Shipliyuk AN, Fedorov AV, Soudakov VG (2012) Stabilization of high-speed boundary layer using porous coatings of various thicknesses. *AIAA J* 50(9):1897–1904. doi:10.2514/1.J051377

- Malik MR (1989) Prediction and control of transition in supersonic and hypersonic boundary layers. *AIAA J* 27(11):1487–1493
- Malmuth N, Fedorov A, Shalaev V, Cole J, Khokhlov A, Hites M, Williams D (1998) Problems in high speed flow prediction relevant to control. In: 2nd AIAA, theoretical fluid mechanics meeting, AIAA 98-2695. doi:[10.2514/6.1998-2695](https://doi.org/10.2514/6.1998-2695)
- Maslov A, Shipliyuk A, Sidorenko A, Polivanov P, Fedorov A, Kozlov V, Malmuth N (2006) Hypersonic laminar flow control using a porous coating of random microstructure. In: 44th AIAA aerospace sciences meeting and exhibit, Reno, Nevada, AIAA 2006-1112
- Maslov AA, Fedorov AV, Bountin DA, Shipliyuk AN, Sidorenko AA, Malmuth N, Knauss H (2008) Experimental study of transition in hypersonic boundary layer on ultrasonically absorptive coating with random porosity. In: 46th AIAA aerospace sciences meeting and exhibit, AIAA, Reno, Nevada, 2008-587
- Ortelt M, Herbertz A, Hald H (2010) Investigations on fibre reinforced combustion chamber structures under effusion cooled LOX/LH2 operation. In: 45th AIAA/ASME/SAE/ASEE joint propulsion conference & exhibit, Denver, CO, AIAA 2009-5475
- Rasheed A, Hornung HG, Fedorov AV, Malmuth ND (2002) Experiments on passive hypervelocity boundary-layer control using an ultrasonically absorptive surface. *AIAA* 40(3):481–489
- Turner J, Hörschgen M, Jung W, Stamminger A, Turner P (2006) SHEFEX hypersonic re-entry flight experiment; vehicle and subsystem design, flight performance and prospects. In: 14th AIAA/AHI space planes and hypersonic systems and technologies conference, AIAA 2006-8115
- Wagner A, Laurence S, Martinez Schramm J, Hannemann K, Wartemann V, Lüdeke H, Tanno H, Ito K (2011) Experimental investigation of hypersonic boundary-layer transition on a cone model in the High Enthalpy Shock Tunnel Göttingen (HEG) at Mach 7.5. In: 17th AIAA international space planes and hypersonic systems and technologies conference, San Francisco, California, USA, AIAA 2011-2374
- Wagner A, Hannemann K, Wartemann V, Tanno H, Ito K (2012) Free piston driven shock tunnel hypersonic boundary layer transition experiments on a cone configuration. In: AVT—specialists’ meeting on hypersonic laminar-turbulent transition, RTO, San Diego, California, USA, RTO-MP-AVT-200
- Wartemann V, Lüdeke H, Sandham ND (2012) Numerical investigation of hypersonic boundary-layer stabilization by porous surfaces. *AIAA J* 50(6):1281–1290
- Wartemann V, Willems S, Gülhan A (2012) Mack mode damping by micropores on a cone in hypersonic flow. In: AVT-200, hypersonic laminar-turbulent transition, San Diego
- Washburn EW (1921) The dynamics of capillary flow. *Phys Rev* 17:273–283. doi:[10.1103/PhysRev.17.273](https://doi.org/10.1103/PhysRev.17.273)
- Weihs H, Longo J, Turner J (2008) Key experiments within the SHEFEX II mission. In: IAC 2008, Glasgow, Scotland UK, IAC-08.D2.6.4
- Willems S, Gülhan A (2012) Damping of the second mode instability with regular and random porous surfaces on a slender cone in hypersonic flow. In: AVT—specialists’ meeting on hypersonic laminar-turbulent transition, San Diego, California, USA